

A SEARCH FOR SUPERSYMMETRY IN EVENTS WITH A Z  
BOSON, JETS, AND MISSING TRANSVERSE ENERGY IN  $p - p$   
COLLISIONS WITH  $\sqrt{s}=13$  TEV WITH THE ATLAS DETECTOR

TOVA RAY HOLMES



Physics Department  
University of California, Berkeley

August 2016 – version 1.0

Tova Ray Holmes: *A Search for Supersymmetry in Events with a Z Boson, Jets, and Missing Transverse Energy in  $p - p$  Collisions with  $\sqrt{s}=13$  TeV with the ATLAS Detector*, © August 2016





## ABSTRACT

---



## PUBLICATIONS

---

Some ideas and figures have appeared previously in the following publications:

Put your publications from the thesis here. The packages `multibib` or `bibtopic` etc. can be used to handle multiple different bibliographies in your document.





## ACKNOWLEDGEMENTS

---

Put your acknowledgements here.



# CONTENTS

---

<b>I</b>	<b>INTRODUCTION</b>	<b>1</b>
1	INTRODUCTION	3
<b>II</b>	<b>THEORY AND MOTIVATION</b>	<b>5</b>
2	THEORY AND MOTIVATION	7
2.1	The Standard Model . . . . .	7
2.1.1	Matter . . . . .	8
2.1.2	Forces . . . . .	9
2.1.3	Phenomenology of Proton-Proton Collisions . .	13
2.1.4	Problems in the Standard Model . . . . .	14
2.2	Supersymmetry . . . . .	16
2.2.1	Supersymmetry Phenomenology . . . . .	16
2.2.2	Solutions to Standard Model Problems . . . . .	16
2.2.3	Supersymmetry Signatures in $p - p$ Collisions .	16
2.3	Monte Carlo Generators . . . . .	16
<b>III</b>	<b>THE EXPERIMENT</b>	<b>17</b>
3	THE LARGE HADRON COLLIDER	19
3.1	Operation of the Large Hadron Collider . . . . .	19
4	THE ATLAS DETECTOR	21
4.1	Coordinate System Used in the ATLAS Detector . . . .	21
4.2	The Inner Detector . . . . .	22
4.2.1	The Pixel Detector . . . . .	22
4.2.2	The Silicon Microstrip Tracker . . . . .	24
4.2.3	The Transition Radiation Tracker . . . . .	24
4.3	The Calorimeters . . . . .	25
4.4	The Muon Spectrometer . . . . .	26
4.5	The Magnet System . . . . .	26
4.6	The Trigger System . . . . .	26
5	OBJECT RECONSTRUCTION IN THE ATLAS DETECTOR	27
5.1	Electrons . . . . .	27
5.2	Photons . . . . .	27
5.3	Muons . . . . .	27
5.4	Jets . . . . .	27
5.5	Missing Transverse Energy . . . . .	27
5.6	Monte Carlo Simulation . . . . .	27
6	APPLICATION OF A NEURAL NETWORK TO PIXEL CLUS- TERING	29
6.1	Clustering in the Pixel Detector . . . . .	29
6.1.1	Charge Interpolation Method . . . . .	30
6.1.2	Improving Measurement with Neural Networks	30
6.2	Impact of the Neural Network . . . . .	31

6.2.1	The Neural Network in 13 TeV Data . . . . .	31
<b>IV</b>	<b>SEARCHING FOR SUPERSYMMETRY</b>	<b>33</b>
7	BACKGROUND PROCESSES	35
7.1	Monte Carlo Samples . . . . .	37
8	OBJECT IDENTIFICATION AND SELECTION	39
8.1	Electrons . . . . .	39
8.2	Muons . . . . .	39
8.3	Jets . . . . .	39
8.4	Photons . . . . .	39
9	EVENT SELECTION	41
9.1	Signal Region . . . . .	41
9.2	Control and Validation Regions . . . . .	41
10	BACKGROUND ESTIMATION	43
10.1	Flavor Symmetric Processes . . . . .	43
10.1.1	Flavor Symmetry Method . . . . .	43
10.1.2	Sideband Fit Method . . . . .	45
10.2	$Z/\gamma^* + \text{jets}$ Background . . . . .	45
10.3	Fakes . . . . .	45
10.4	Dibosons . . . . .	45
10.5	Other Rare Processes . . . . .	45
11	SYSTEMATIC UNCERTAINTY	47
11.1	Uncertainties on Data-Driven Backgrounds . . . . .	47
11.1.1	Uncertainties on the Flavor Symmetry Method . . . . .	47
12	RESULTS	51
13	INTERPRETATIONS	53
<b>V</b>	<b>CONCLUSIONS</b>	<b>55</b>
14	CONCLUSIONS	57
15	OUTLOOK	59
<b>VI</b>	<b>APPENDIX</b>	<b>61</b>
A	APPENDIX TEST	63
A.1	Appendix Section Test . . . . .	63
A.2	Another Appendix Section Test . . . . .	64
	BIBLIOGRAPHY	65

## LIST OF FIGURES

Figure 1	The Standard Model of particle physics, containing all known bosons and fermions, with the addition of the hypothetical graviton. [19]	8
Figure 2	The running of the strong coupling constant, $\alpha$ . [26]	12
Figure 3	2008 MSTW Parton Distribution Functions (PDFs) for various particle types. [25]	14
Figure 4	Galactic rotation curve showing that the discrepancy between the observed luminous matter and the total mass in the system can be described as a non-luminous halo of matter. [29]	15
Figure 5	Diagram of the ATLAS detector, with subsystems and magnets identified.	21
Figure 6	Diagram of the ATLAS Inner Detector, containing the Pixel, SCT, and TRT subsystems.	23
Figure 7	Diagram of one-quarter of the ATLAS Inner Detector, with lines drawn to indicate various $\eta$ locations. The labels PP <sub>1</sub> , PPB <sub>1</sub> and PPF <sub>1</sub> indicate the patch-panels for the ID services. TODO: what is that.	24
Figure 8	The calorimeter system of the ATLAS detector.	25
Figure 9	A few possible types of clusters in the Pixel Detector. (a) shows a single particle passing through a layer of the detector, (b) shows two particles passing through the detector, creating a single merged cluster, and (c) shows a single particle emitting a $\delta$ -ray as it passes through the detector.	29
Figure 10	One example of a two-particle cluster and its truth information compared with the output of the Neural Networks (NNs). At top, the $p(N = i)$ values give the output of the Number NN, the probabilities that the cluster contains 1, 2, and 3 particles. Given the highest probability is for $N = 2$ , the other NNs predict the position and errors of the two particles (in white). The black arrows and squares represent the truth information from the cluster, and the black dot and dotted line show the position measurement for the un-split cluster.	32

Figure 11	$x$ resolutions for clusters with 3 (left) and 4 (right) pixels in the $x$ direction in $7\text{TeV}$ data for Connected Component Analysis (CCA) and NN clustering. . . . .	32
Figure 12	An example Feynman diagram of $t\bar{t}$ production and decay. . . . .	35
Figure 13	An example Feynman diagram of the production and decay of a WZ event. . . . .	36
Figure 14	An example Feynman diagram of the production and decay of a $Z/\gamma^* + \text{jets}$ event. . . . .	36
Figure 15	MC closure plots of VRS (top) and SRZ (bottom). The number of events from MC (black points) is compared to the number of events predicted from the flavor symmetry method (yellow histogram). The comparison is performed before the expanded $m_{\ell\ell}$ window is used to predict the on-Z bin. . . . .	49
Figure 16	Measurements of $k$ , the ratio of electron to muon events, in bins of $p_T$ and $\eta$ . On the left is the measurements indexed by the leading lepton, while the measurements indexed by the sub-leading lepton are on the right. . . . .	50

## LIST OF TABLES

Table 1	Simulated background event samples used in this analysis with the corresponding matrix element and parton shower generators, cross-section order in $\alpha_s$ used to normalise the event yield, underlying-event tune and PDF set. . . . .	38
Table 2	Overview of all signal, control and validation regions used in the on-shell Z search. More details are given in the text. The flavour combination of the dilepton pair is denoted as either “SF” for same-flavour or “DF” for different flavour. All regions require at least two leptons, unless otherwise indicated. In the case of $\text{CR}\gamma$ , VR-WZ, VR-ZZ, and VR-3L the number of leptons, rather than a specific flavour configuration, is indicated. The main requirements that distinguish the control and validation regions from the signal region are indicated in bold. Most of the kinematic quantities used to define these regions are discussed in the text. The quantity $m_T(\ell_3, E_T^{\text{miss}})$ indicates the transverse mass formed by the $E_T^{\text{miss}}$ and the lepton which is not assigned to either of the Z-decay leptons. . . . .	41
Table 3	List of the triggers considered for this analysis. The corresponding L1 items are included for reference. The last column notes if the trigger is available in data. . . . .	42
Table 4	Lepton trigger requirements used for the analysis in different regions of lepton- $p_T$ phase space. 42	
Table 5	Yields in signal and validation regions for the flavor symmetric background. Errors include statistical uncertainty, uncertainty from MC closure, uncertainty from the k and $\alpha$ factors, uncertainty due to deriving triggers efficiencies from a DAOD, and uncertainty on the MC shape used to correct for the $m_{\ell\ell}$ expansion. . . . .	45

Table 6	Uncertainties in the on-Z signal and validation regions. Nominal predictions are given with statistical uncertainty (including uncertainty from subtracted backgrounds), MC Closure uncertainty, uncertainty on the prediction from varying $k$ and $\alpha$ by their statistical uncertainties, comparing the efficiencies from AODs to that of DAODs, and on the $m_{\ell\ell}$ widening, which includes MC statistics and a data/MC comparison in a loosened region. . . . .	48
Table 7	Autem usu id . . . . .	64



## LISTINGS

---

Listing 1	A floating example (listings manual) . . . . .	64
-----------	--	----

## ACRONYMS

---

LHC	Large Hadron Collider
IBL	Insertable B-Layer
MS	Muon Spectrometer
ID	Inner Detector
SCT	Silicon Microstrip Tracker
TRT	Transition Radiation Tracker
NN	Neural Network
CCA	Connected Component Analysis
ToT	Time Over Threshold
MC	Monte Carlo simulation
SM	Standard Model
BSM	Beyond the Standard Model
SUSY	Supersymmetry
QCD	Quantum Chromodynamics
PDF	Parton Distribution Function
DM	Dark Matter
MC	Monte Carlo
AOD	Analysis Object Data
SR	Signal Region
VR	Validation Region
CR	Control Region
FS	Flavor Symmetric

## Part I

### INTRODUCTION

The centerpiece of this thesis is a search for Supersymmetry, but it also includes all the scaffolding and background necessary to understand the search. An overview of the Large Hadron Collider ([LHC](#)) and the ATLAS Detector are presented along with the theory that motivates the search.



## INTRODUCTION

---

The pages that follow detail the author's work on the ATLAS experiment from 2011 through 2016, focusing on an analysis of  $13\text{TeV}$  proton-proton collisions at the [LHC](#) looking for Supersymmetry with the ATLAS Detector.

CHAPTER 2 outlines the Standard Model of Particle Physics and the benefits of extending it to include Supersymmetry, then continues to describe the motivation behind searching for this particular model.

CHAPTER 3 describes the [LHC](#) and its operation.

CHAPTER 4 contains descriptions of the many pieces of the ATLAS detector, and how they serve to detect particles coming from [LHC](#) collisions.

CHAPTER 5 presents a neural network designed to improve tracking in the ATLAS Pixel Detector, and describes the benefits of its implementation.



## Part II

### THEORY AND MOTIVATION

This section describes the theoretical foundation for the analysis presented in [Part iv](#). It includes an overview of the Standard Model, including its phenomenology in a  $p - p$  collider. The theory of Supersymmetry is explained, and the motivation for extending the Standard Model to include it is presented. In addition, this section includes an explanation of Monte Carlo generators and details about the specific form of Supersymmetry searched for in this analysis.





The Standard Model (SM) of particle physics represents all particles and interactions currently understood by the particle physics community. It is formulated using the principles of Quantum Field Theory, with the constraints of several symmetries and physical requirements to determine the rules for allowed interactions. [11] Developed in the 1960s and 70s, it has been immensely successful at predicting additional particles, and has held up to many high-precision tests. Despite this success, it has several shortcomings which point to its incompleteness. Though the SM is likely correct at the energies thus far probed, it may be missing key components that become more important at higher energies. Models supplementing the SM with additional particles and interactions are referred to as Beyond the Standard Model (BSM) theories.

One possible extension of the SM is Supersymmetry (SUSY), a theory which applies an additional symmetry between bosons and fermions to the SM, creating a spectrum of SUSY particles (sparticles) which interact with the particles of the SM. This theory motivates the search performed in Part iv, and its theoretical appeals are discussed in this section, along with specific simplified models considered in the search.

## 2.1 THE STANDARD MODEL

The SM of particle physics describes the interactions of all of the particles currently known to exist, and consists of both matter particles and force carriers. This model has been unprecedentedly successful in predicting new particles and phenomena, including the prediction of the Higgs particle almost 50 years before its discovery in 2012, which completed the SM. This section describes the components of the SM and how they interact, focusing on the environment of the LHC.

The particles of the SM are divided into two categories: fermions and bosons. The fermions comprise all the matter described by the SM, and are spin- $\frac{1}{2}$  particles. The bosons, integer-spin particles, are the force carriers. They provide a mechanism to explain three of the four forces known to particle physics, with gravity still lacking a quantum formalization. The Higgs boson, the only spin-0 particle in the SM, provides a mechanism for giving mass to the other particles. The full SM, with the addition of the hypothetical graviton, is presented in Figure 1.

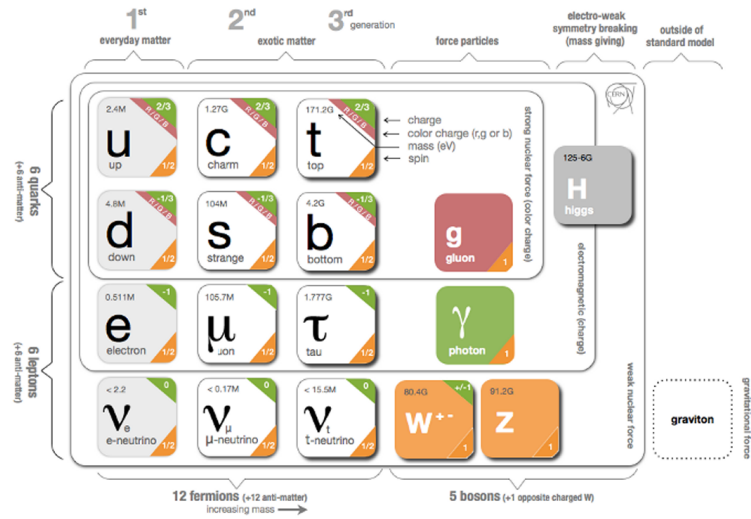


Figure 1: The Standard Model of particle physics, containing all known bosons and fermions, with the addition of the hypothetical graviton. [19]

### 2.1.1.1 Matter

The matter described by the SM is made up of fermions, spin- $\frac{1}{2}$  particles which can be broken into two groups, quarks and leptons. The leptons all interact weakly, while the quarks additionally interact strongly.

#### 2.1.1.1.1 Leptons

Leptons, as seen in the bottom left of Figure 1, come in three generations, each labeled by a flavor: electron, muon, and tau. In the case of the massive leptons, these flavors are mass eigenstates, and the generations are placed in an order based on increasing mass. Each massive lepton is negatively charged and has a positively charged anti-particle.

The three neutrinos come in the same flavors as the massive leptons, but these flavor eigenstates do not correspond exactly to mass eigenstates. As a consequence, neutrinos oscillate between flavors as they propagate through space. These oscillations are the only evidence of neutrino mass, which is bound from below by the mass splittings determined from the oscillation. Though it is still uncertain if the masses of the neutrinos follow the same hierarchy as the massive leptons, that expected ordering is slightly preferred over the inverted hierarchy. [22]

Unlike the massive leptons, the neutrinos are uncharged, and it is not yet known whether each neutrino has a separate anti-particle, or if it is its own antiparticle. Because they are uncharged, they can only interact weakly, making them extremely difficult to detect. In the AT-

LAS detector, neutrinos pass through all layers undetected, and their presence can only be inferred from the non-conservation of momentum that results in the observed particles. As a consequence of their ability to evade detection, neutrinos are the least understood particles of the SM.

The SM conserves lepton number,  $L$ , which is defined as the number of leptons minus the number of anti-leptons in a state. While this conservation is not theoretically required, its violation has not yet been observed. As a consequence of this conservation, the lightest massive lepton, the electron, is stable.

#### 2.1.1.2 Quarks

Quarks, as seen in the top left of Figure 1, are also charged particles that interact weakly, but are differentiated from the leptons by their strong interactions. They are also organized in three generations ordered by mass, and come in pairs of “up-type” and “down-type” quarks, named after the lightest generation. Though the up quark is lighter than the down, that rule is reversed in the subsequent two generations. Up-type quarks are charged  $+\frac{2}{3}$ , while the down-type quarks are charged  $-\frac{1}{3}$ . Quarks are also charged under the strong interaction, whose three charges are often characterized by colors: red, green, and blue. Each quark has an anti-particle with the opposite charges.

These fractional charges and individual colors are never seen in nature because of the requirement (discussed further in Section 2.1.2.2) that stable particle states be color-neutral. To accomplish this, quarks can create two-particle bound states called *mesons* consisting of one quark and one anti-quark with the same color charge or three-particle bound states of quarks or anti-quarks with the three different color charges, which are called *baryons*. The lightest color neutral state containing only quarks, the proton ( $uud$ ), is stable. Extremely unstable bound states consisting of higher numbers of quarks can also exist, such as the pentaquark discovered in 2015 at the LHC. [28] Collectively, these multi-quark bound states are called *hadrons*.

Like leptons, the number of quarks in a state is conserved. However, because quarks cannot exist in an isolated state, that conservation described as a conservation of baryon number ( $B$ ) defined similarly to lepton number. Mesons, because they have one quark and one anti-quark, have  $B = 0$ .

#### 2.1.2 Forces

The fermions in the previous section interact via the electromagnetic, weak, and strong forces. In a perturbative quantum field theory, interactions via these forces are represented by mediating bosons. These force carriers interact only with particles charged with their force's

quantum numbers. The photon, for example, interacts only with electromagnetically charged particles. Gluons, mediators of the strong force, interact only with color charged particles, quarks and gluons. All fermions are weakly charged and interact with the weak force's mediators, the  $W$  and  $Z$  bosons.

The formulation for each of these forces is developed by requiring that the [SM](#) lagrangian be locally gauge invariant. [21] This can be accomplished by adding gauge fields to the lagrangian, whose behavior under gauge transformations cancels out the gauge dependence of the free lagrangian. However, adding a mass term for these fields reintroduces gauge dependence, so this mechanism only creates forces mediated by massless particles.

### 2.1.2.1 The Electromagnetic Force

The simplest example of gauge invariance requirements generating a description of a force can be found in electromagnetism. It has one massless mediator, the photon, which interacts with all electromagnetically charged particles. What follows is a brief description of how enforcing this invariance generates a lagrangian of the same form as the classical electromagnetic lagrangian, which can be easily incorporated into the [SM](#).

The particles in [Section 2.1.1](#) are fermions, and so their free lagrangians are Dirac lagrangians and all follow the form

$$\mathcal{L} = i\bar{\psi}\gamma^\mu\partial_\mu\psi - m\bar{\psi}\psi. \quad (1)$$

Requiring that the free lagrangians for these particles be invariant under a  $U(1)$  local gauge transformation,  $e^{iq\lambda(x)}$ , can be accomplished by adding a term to the lagrangian which cancels the derivative term arising from  $\lambda$ 's dependence on  $x$ :

$$\mathcal{L} = i\bar{\psi}\gamma^\mu\partial_\mu\psi - m\bar{\psi}\psi - (q\bar{\psi}\gamma^\mu\psi)A_\mu \quad (2)$$

where  $A_\mu$  is a “gauge field” that transforms according to

$$A_\mu \rightarrow A_\mu + \partial_\mu\lambda. \quad (3)$$

This vector field must also come with a free term,

$$\mathcal{L} = -\frac{1}{16\pi}F^{\mu\nu}F_{\mu\nu} + \frac{1}{8\pi}m_A^2A^\nu A_\nu. \quad (4)$$

The mass term for this field would not itself be invariant under the transformation, but the field can simply be made massless to avoid this problem. The final lagrangian, then, is

$$\mathcal{L} = i\bar{\psi}\gamma^\mu\partial_\mu\psi - m\bar{\psi}\psi - \frac{1}{16\pi}F^{\mu\nu}F_{\mu\nu} - (q\bar{\psi}\gamma^\mu\psi)A_\mu \quad (5)$$

which is precisely the original lagrangian with the addition of terms replicating the form of the Maxwell lagrangian. In a quantized interpretation, it describes a field that interacts with particles with non-zero electromagnetic charge  $q$  via interactions with a massless spin-1 boson, the photon.

For the purpose of succinct notation, this lagrangian is often rewritten in terms of the “covariant derivative”

$$\mathcal{D}_\mu = \partial_\mu + iq\lambda A_\mu \quad (6)$$

which immediately cancels the gauge dependent term created by the transformation. This mechanism is mathematically simple in the  $U(1)$  case, but can be replicated for more complicated gauge transformations with perturbative approximations.

### 2.1.2.2 Quantum Chromodynamics

Quantum Chromodynamics (QCD), the theory describing the strong force, can be formulated similarly to the electromagnetic force, but with a  $SU(3)$  transformation replacing  $U(1)$ . This transformation acts on a vector of equal mass quarks, the three different colors of a given flavor. The transformation is written as follows,

$$\psi \rightarrow e^{-iq\lambda \cdot \phi(x)} \psi \quad (7)$$

where  $\phi$  gives a vector of coefficients to be multiplied by the Gell-Mann matrices,  $\lambda$ . Though the math is more complicated than the  $U(1)$  case in this higher dimensional rotation, the cancellation is ultimately similar.

The main difference, corresponding to this more complicated basis of transformations, is that eight fields  $A_\mu$  are required rather than the one needed in electromagnetism. These eight fields correspond to eight massless bosons, the different color states of the gluon, the carrier of the strong force.

All together, the total lagrangian for QCD is

$$\mathcal{L} = i\bar{\psi}\gamma^\mu\partial_\mu\psi - m\bar{\psi}\psi - \frac{1}{16\pi}\mathbf{F}^{\mu\nu}\mathbf{F}_{\mu\nu} - (q\bar{\psi}\gamma^\mu\psi)\mathbf{A}_\mu, \quad (8)$$

an equation identical in form to Equation 5, with the mathematical complications of the additional fields hidden by the vector notation. In addition to that change, the covariant derivative must accommodate a vector  $\mathbf{A}$  as well, changing only slightly to be defined as

$$\mathcal{D}_\mu = \partial_\mu + iq\lambda \cdot \mathbf{A}_\mu. \quad (9)$$

This canceling is actually only satisfied to a first order expansion of the transformation, guaranteeing its validity only for infinitesimally small  $\phi$ . However, the strong coupling constant,  $\alpha$ , depends on the energy scale of the interaction, decreasing at higher energy scales and asymptotically increasing at low energies. Figure 2 shows this effect translated to distance scales, demonstrating that QCD is weak and can be considered perturbatively at small distance scales, but at large distance scales this approximation breaks down, and the colorless hadrons introduced in Section 2.1.1.2 must be used to describe interactions instead. The boundary between these regimes is referred to as  $\Lambda_{\text{QCD}}$ .

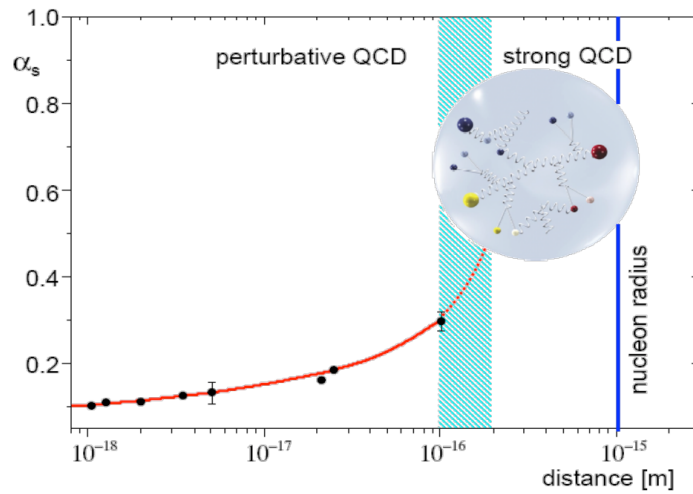


Figure 2: The running of the strong coupling constant,  $\alpha$ . [26]

### 2.1.2.3 The Weak Force

A similar process, using an  $SU(2)$  gauge transformation, can produce a lagrangian that would suffice to describe the  $W$  and  $Z$  bosons of the SM, if only they were massless. However, they are not, so an alternate mechanism must be used to add masses to the lagrangian.

Before a mechanism for their masses was understood, and before they were discovered, the large mass of the  $W$  and  $Z$  bosons were proposed in order to unify the electromagnetic and weak forces into the electroweak force. The large masses were crucial to explain the discrepancy in the strength of the two forces.

This unified theory resulted in a triplet,  $\mathbf{W}$ , with coupling  $g_W$ , and a singlet field  $B$ , with coupling  $g'/2$ . However, this electroweak symmetry is broken, and mixing between these states occurs. Rewritten in their mass basis, the more familiar electroweak force carriers are produced:  $W^\pm$ , two states with identical coupling,  $Z^0$ , and  $A$ , the photon field.

#### 2.1.2.4 The Higgs Mechanism

The reason for this symmetry breaking has to do with the final piece of the [SM](#), the Higgs boson. The Higgs mechanism presents an alternate way to generate a mass term, through an unexpected route. It is a scalar field, with a lagrangian

$$\mathcal{L} = \frac{1}{2}(\partial_\mu \phi)^*(\partial^\mu \phi) + \frac{1}{2}\mu^2 \phi^* \phi - \frac{1}{4}\lambda^4 (\phi^* \phi)^2 \quad (10)$$

where  $\phi$  is a complex scalar field,  $\phi = \phi_1 + i\phi_2$ . This looks very similar to the standard scalar field, but the signs on the mass and interaction terms are reversed, giving a result that looks like an imaginary mass. However, this lagrangian differs from all previously considered lagrangians in that its ground state does not occur at  $\phi = 0$ . Because this is a perturbative theory, its validity only holds when expanded around the ground states, which must satisfy

$$\phi_1^2 + \phi_2^2 = -\frac{\mu}{\lambda}. \quad (11)$$

Rewriting the original lagrangian in terms of fields centered around ground states chosen to satisfy that condition results in a reasonable mass term. However, in an effect called “spontaneous symmetry breaking”, the original  $SO(2)$  rotational symmetry of the lagrangian is lost, resulting only in a  $U(1)$  rotational symmetry; the lagrangian is invariant under a phase transformation.

As in [Section 2.1.2.1](#), it is possible to make the lagrangian invariant under a local  $U(1)$  transformation,  $\phi \rightarrow e^{i\theta(x)}\phi$  by adding a massless gauge field  $A^\mu$  and using the covariant derivative. Due to the many cross terms from the non-zero ground state, terms for the mass of one of the bosons as well as the gauge field appear, leaving only one massless boson. The massless boson, it turns out, can be completely removed from the theory via local  $U(1)$  transformations, ultimately producing a theory with one massive scalar (the Higgs) and a massive gauge field.

#### 2.1.3 Phenomenology of Proton-Proton Collisions

As discussed in [Chapter 3](#), the [LHC](#) collides bunches of high-energy protons, and the interactions of these protons’ constituent quarks produce the wide array of particles seen in the ATLAS detector. The [LHC](#) typically cites its energy in terms of  $\sqrt{S}$ , the center of mass energy of protons in the two colliding beams. However, because the proton is not fundamental, this energy is divided among many particles that make up the proton.

To first order, a proton consists of three quarks: two up quarks and one down quark. However, a real quantum mechanical system is



much more chaotic, with other quarks popping into and out of existence and gluons flying between them. These additional quarks are called “sea” quarks. The particles inside the proton can have a wide range of energies depending on the internal dynamics at the moment of the collision. These cannot be predicted exactly, but probabilistic models called **PDFs** describe the likelihood of any given configuration. These models are determined using data from hard scattering experiments and give probabilistic estimates for how often a given type of particle appears with a fraction  $x$  of the total proton energy, as seen in Figure 3.

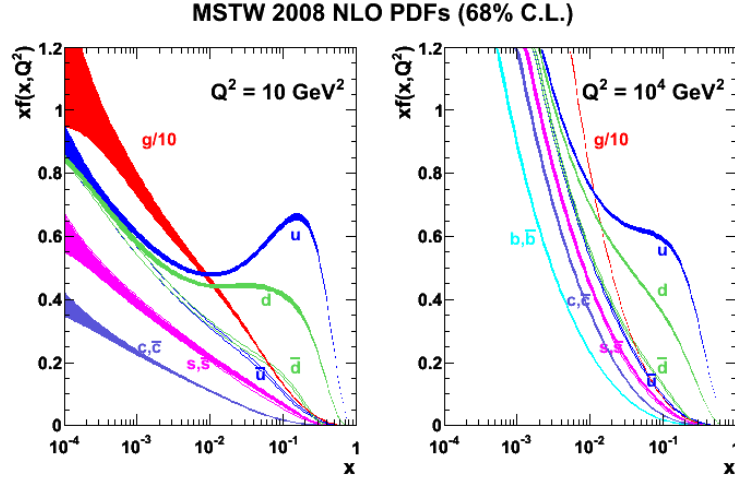


Figure 3: 2008 MSTW **PDFs** for various particle types. [25]

#### 2.1.4 Problems in the Standard Model

Though the **SM** is a self-consistent theory that describes to great accuracy all of the particles and forces it includes, it does have certain shortcomings. The most glaring is the omission of gravity. Though the force is well understood at large scales via the theory of General Relativity, no satisfying quantum description of gravity has been accepted, much less proven. The Planck scale, the energy scale at which gravitational interactions become large enough that no sound theory can ignore gravity, is at about  $10^{28}$  eV, 16 orders of magnitude above the electroweak scale.

Another clear omission of the **SM** is Dark Matter (**DM**). This matter was first identified in 1933 through the observation of galactic rotation curves. [27] The speed of rotation indicated both that there was more mass in the system than could be accounted for by observations made directly of the galaxy, and that this additional matter was distributed in a halo, not a disk like the typical luminous matter. This effect can be seen in Figure 4. Since then, the gravitational impact of **DM** has been observed in colliding clusters and many more rotational



curves, but it has never been directly detected or seen at a particle accelerator. As a consequence, very few details are known about the nature of the particles that make up this matter, only that it does not interact strongly or electromagnetically and its density throughout the universe.

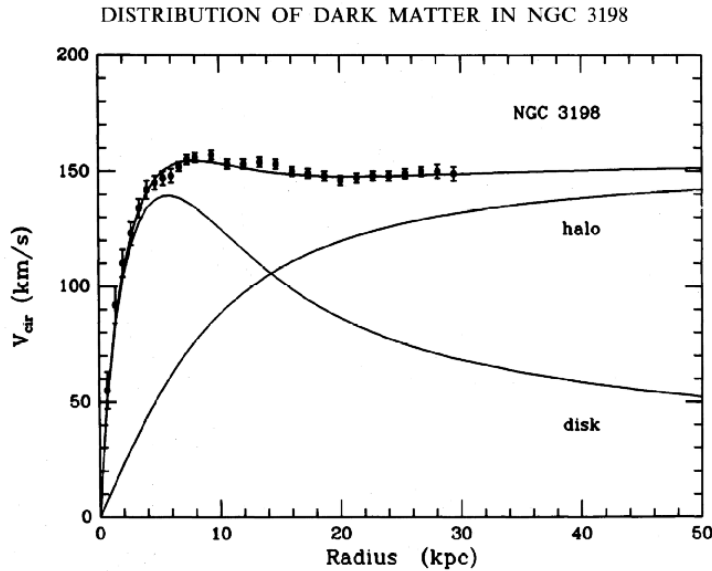


Figure 4: Galactic rotation curve showing that the discrepancy between the observed luminous matter and the total mass in the system can be described as a non-luminous halo of matter. [29]

Beyond the omissions of the SM, there are several aesthetic problems - things that could have no solution, but seem to suggest that the current SM are missing some pieces that could unify it and provide more order. The first is the sheer number of parameters in the SM. There are 26 independent parameters determining the mass of the particles and all the couplings between them. Besides the rough grouping of fermions into generations, there seems to be no order to masses of particles, and no way to predict the masses or couplings. Each, it seems, is independently provided by nature.

In the past, large numbers of seemingly unrelated parameters has indicated that a theory has a more fundamental form at shorter distance scales. The large number of elements, it turned out, could be explained by different groupings of three particles, the proton, neutron and electron. Later, the menagerie of hadrons became so large that a similar reimagining of what was fundamental took place, and the theory of quarks gave an order to the many mesons and baryons. This pattern leaves physicists suspicious of any theory with too many particles and free parameters, suggesting that perhaps, at a higher energy, there is a simpler model that can unify many of the seemingly disparate elements of the SM.

However, some of these seemingly independent parameters have suspicious symmetry. The Higgs mass, for example, has been measured to be 125 GeV. This mass is the sum of the bare mass, the one that appears in the lagrangian, and quantum corrections from interactions with other particles, which are proportional to the square of the particles' mass. Since new physics must exist at the Planck scale to account for gravity, these corrections could be up to 35 orders of magnitude larger than the Higgs mass. The bare mass could theoretically cancel out this massive correction, these parameters should be independent, and the odds that they would be precisely the same to 35 places are very, very small. This exact canceling is often called “fine-tuning”, an undesirable trait in a theory which suggests that some more fundamental symmetry has been missed. The word “naturalness” is used to describe the the extent to which a theory is free of fine-tuning.

## 2.2 SUPERSYMMETRY

### 2.2.1 *Supersymmetry Phenomenology*

### 2.2.2 *Solutions to Standard Model Problems*

Many believe that a complete [SM](#) would include a unification of the three forces, as electromagnetism and the weak force have already been unified. This requires that at some higher energy, the coupling constants of all three forces merge.

### 2.2.3 *Supersymmetry Signatures in $p - p$ Collisions*

#### 2.2.3.1 *Simplified Models Used in This Analysis*

## 2.3 MONTE CARLO GENERATORS

## Part III

### THE EXPERIMENT

This section describes the [LHC](#) and the ATLAS detector, which collectively provide the physical environment and the data collection for the analysis discussed in [Part iv](#).



## THE LARGE HADRON COLLIDER

---

The [LHC](#) is unique in the world, producing proton-proton collisions at energies an order of magnitude higher than any accelerator before. It provides unique environments at its collision points where massive, unstable particles can exist for an instant, then decay to the ordinary material of the universe. It is the goal of the ATLAS experiment to identify these short-lived particles, but [LHC](#)'s work of producing them is equally complex.

### 3.1 OPERATION OF THE LARGE HADRON COLLIDER



## THE ATLAS DETECTOR

The ATLAS detector circumscribes the LHC's beam pipe, enclosing the collision point with a series of particle detecting layers, aimed at making as many measurements of the particles leaving the collision point as possible. Its goal is to get a precise measurement of all the stable or semi-stable particles flying from proton-proton collisions at its center, allowing analyzers to fully reconstruct the kinematics of the underlying processes.

The ATLAS detector is the largest detector of its kind, measuring 44 m in length and 25 m in height, as seen in Figure 5. The size is mainly determined by the constraints of the Muon Spectrometer (MS), discussed in Section 4.4, which is the largest and outermost subsystem. The MS is submerged in a spatially varying magnetic field provided by three toroidal magnets, while the Inner Detector (ID) (Section 4.2) is encased by a superconducting solenoid, which provides a uniform 2 T field throughout its volume [1].

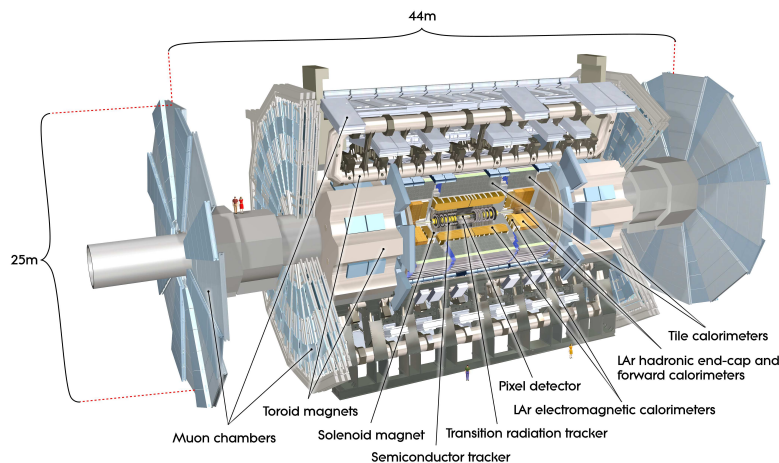


Figure 5: Diagram of the ATLAS detector, with subsystems and magnets identified.

### 4.1 COORDINATE SYSTEM USED IN THE ATLAS DETECTOR

The ATLAS detector is centered around the collision point in the beam pipe, and is built radially out from the pipe, maintaining as much rotational symmetry as possible. It is also symmetric in the forward-backward directions. Because of this geometry, a coordinate system using the collision point as the origin is used, with the beam

pipe defining the  $z$ -axis. The positive  $x$  direction is defined as pointing to the center of the LHC ring, while the positive  $y$  direction points upwards. For ease of reference, the side of the detector in the positive- $z$  direction is referred to as the A side, and the other side is referred to as the C side.

Because of the radial design of the detector, angular coordinates are often used. The azimuthal angle  $\phi$  defines the radial distance around the beam pipe and the polar angle  $\theta$  defines the angle from the beam axis ( $z$ ). However, a transformation of the polar angle called pseudorapidity ( $\eta$ ) is used more often, and is defined as

$$\eta = -\ln\left[\tan\frac{\theta}{2}\right]. \quad (12)$$

Building on this variable definition, distance between objects is typically defined as

$$\Delta R = \sqrt{\Delta\eta^2 + \Delta\phi^2}. \quad (13)$$

Often variables are defined purely in the transverse plane, which is indicated by a subscripted  $T$ , as in  $p_T$ , which gives an object's transverse momentum. Another common usage is  $E_T^{miss}$ , which gives the negative vectorial sum of the energy in an event.

## 4.2 THE INNER DETECTOR

One goal of the ATLAS detector is to produce tracks, predictions of the paths particles take as they travel through the detector. Collisions in the detector produce about 1000 particles, so identifying and differentiating all these tracks is both a hardware and a computational challenge. The ID, also called the Tracker, is responsible for providing high enough resolution measurements that each of these tracks and its precise position can be recorded. This tracking system consists of three subdetectors which each produce electrical responses to charged particles passing through their active material. Each of these signals is called a hit. ATLAS tracking software considers all these hits and forms tracks, with the goal of minimizing fake tracks due to random noise. Some details of this process is discussed at length in Chapter 6. The full ID can be seen in Figure 6, while a schematic in Figure 7 demonstrates the  $\eta$  coverage of each detector.

### 4.2.1 The Pixel Detector

The Pixel detector lies closest to the beam pipe of the LHC, and has four layers comprising 92 million read-out channels. There are three



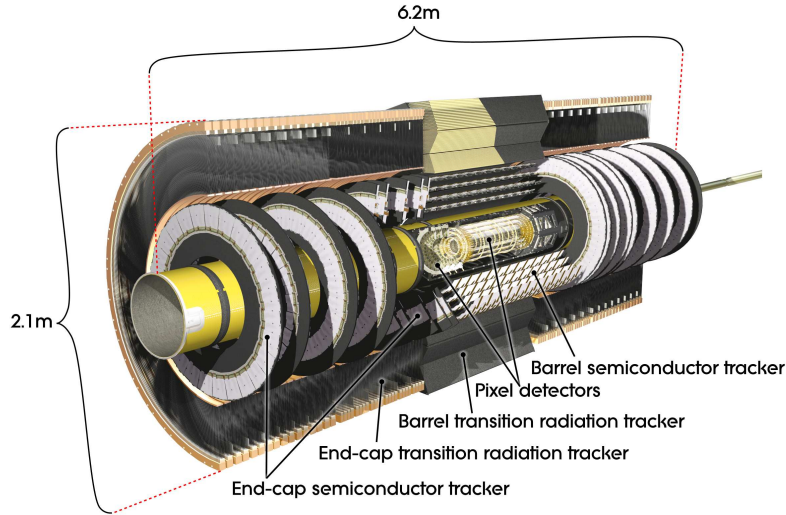


Figure 6: Diagram of the ATLAS Inner Detector, containing the Pixel, SCT, and TRT subsystems.

standard layers, referred to as Layers 1-3 (L1, L2, L3), and an additional layer added for the 2015 data-taking, called the Insertable B-Layer (IBL).

#### 4.2.1.1 The Original Pixel Detector

The Pixel Detector consists of high-precision silicon chip pixel sensors, with 1744 sensors total. Each sensor is identical, containing 47232 pixels, which are typically each  $50 \times 400 \mu\text{m}^2$ .

As shown in Figure 7, the central  $\eta$  region (barrel) is covered by three concentric cylindrical layers of sensors, while the higher  $\eta$  region (endcap) is covered by a series of three disks positioned in the  $x - y$  plane. Together, they give complete coverage out to  $\eta = 2.5$ , and a particle coming from the collision point will typically be measured by three layers. Each of these measurements is accurate in the barrel (endcap) to  $10 \mu\text{m}$  in the  $R - \phi$  direction and  $115 \mu\text{m}$  in the  $z$  ( $R$ ) direction.

#### 4.2.1.2 Addition of the IBL

In 2015, the IBL was lowered into the ATLAS cavern and added to the Pixel Detector. This layer sits on top of the beam pipe, inside barrel L1, which was formerly responsible for the first measurement of charged particles coming from a collision. TODO: add info about precision

As the IBL's name suggests, it was added to improve detection of  $B$  mesons, whose non-trivial lifetimes create secondary vertices in ATLAS events, which allow them to be distinguished from other particles with precise track measurement. The IBL is closer to the interaction point and has a smaller resolution, giving it a better chance to see these slightly displaced vertices.

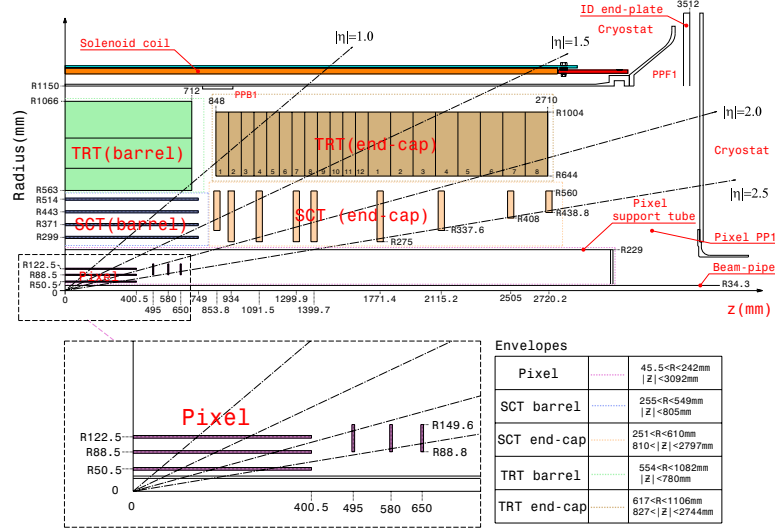


Figure 7: Diagram of one-quarter of the ATLAS Inner Detector, with lines drawn to indicate various  $\eta$  locations. The labels PP1, PPB1 and PPF1 indicate the patch-panels for the ID services. TODO: what is that.

#### 4.2.2 The Silicon Microstrip Tracker

The Silicon Microstrip Tracker (SCT) employs similar technology to the Pixel Detector, with 15912 sensors and 6.3 million readout channels. Its difference from the Pixel Detector is in the readout, which is performed by a series of 12 cm long strips with a width of  $80 \mu\text{m}$ . These layers are paired, placed on top of one another at a small ( $40 \text{ mrad}$ ) angle to allow for position determination in both directions, giving 4 spatial measurements for each particle passing through the SCT. In the barrel, these strips run parallel to the beam pipe, while in the endcap, they are arranged radially. These strips have a resolution in the barrel (endcap) of  $17 \mu\text{m}$  in the  $R - \phi$  direction and  $580 \mu\text{m}$  in the  $z$  ( $R$ ) direction.

#### 4.2.3 The Transition Radiation Tracker

The Transition Radiation Tracker (TRT) uses 4mm diameter gas-filled tubes, each with a high voltage wire suspended along the center of the tube. The tubes run the length of the barrel, with a separate wire in the positive and negative  $z$  direction. In the endcap, the tubes are arranged radially. In total, there are about 351,000 readout channels in the TRT. This detector makes measurements only in the  $R - \phi$  direction, where the resolution of each measurement is  $130 \mu\text{m}$ . Each particle typically creates about 36 hits as it passes through the TRT.

TODO is any of this right? Particles passing through the gas mixture of the TRT ionize the gas, producing electrons which drift towards

the wire due to a potential difference applied between it and the straw. This process takes about 48 ns, and the signal can be directly read out, giving the fastest measurement of particles in the ID. This speedy readout is essential to triggering, discussed more in [Section 4.6](#).

The TRT also responds to low-energy transition radiation photons, which produce a much larger signal than charged particles passing through the detector. Because of this strong difference in signals, hits from the TRT are used to help differentiate between electrons and photons in the detector.

### 4.3 THE CALORIMETERS

Unlike the tracking detectors, which aim to take measurements of a particle with minimal alterations of its trajectory, the calorimeters measure the energy of objects by stopping them entirely. The calorimeters, which can be seen in [Figure 8](#), provide coverage out to  $\eta < 4.9$ . Higher granularity electromagnetic measurements are made within  $|\eta| < 2.5$ , where the ID provides tracking capability, in order to give precision measurements of the energy of photons and electrons, and provide reduced resolution measurements at higher  $\eta$ . The hadronic calorimeters provides coarser granularity, which is sufficient to determine the energy of jets.

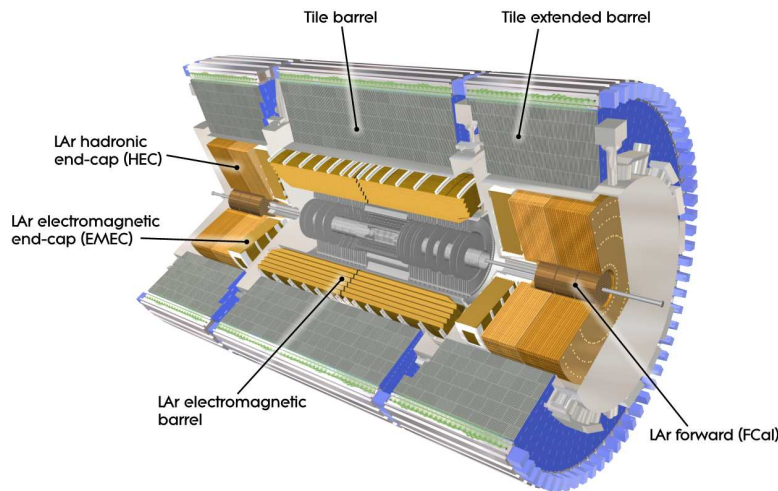


Figure 8: The calorimeter system of the ATLAS detector.

TODO make sure jets are in theory.

Another task of the calorimeter system is to limit punch-through to the MS, described in [Section 4.4](#). All other particles must be fully stopped by the calorimeters to allow for clean signals from muons, and to measure the total energy of the particle. This requirement sets minimum sizes for each of the calorimeters.

THE LAR ELECTROMAGNETIC CALORIMETER uses liquid argon as its active detector medium alternating with layers of lead acting as the absorber. The layers are shaped like accordions, which allows for complete coverage with multiple layers of active material, three in central  $\eta$  ( $0 < |\eta| < 2.5$ ) and two at higher  $\eta$  ( $2.5 < |\eta| < 3.2$ ). At  $|\eta| < 1.8$ , an instrumented liquid argon presampler provides a measurement of energy lost prior to reaching the calorimeters.

THE TILE CALORIMETER is a hadronic calorimeter which surrounds the LAr Calorimeter. It uses layers of steel as its absorber with scintillating tiles as the active material between them, which are read out by photomultiplier tubes. The Tile Calorimeter covers  $|\eta| < 1.7$ .

THE LAR HADRONIC ENDCAP CALORIMETER covers the hadronic calorimetry for higher  $\eta$ . It uses liquid argon active material and copper plate absorbers. This calorimeter covers  $1.5 < |\eta| < 3.2$ , overlapping with the hadronic calorimeters in either direction of its  $\eta$  range.

THE FCAL or forward calorimeter provides electromagnetic and hadronic coverage at very high  $\eta$  ( $3.1 < |\eta| < 4.9$ ). This calorimeter also uses liquid argon as its active material, and uses copper-tungsten as the absorber.

#### 4.4 THE MUON SPECTROMETER

#### 4.5 THE MAGNET SYSTEM

#### 4.6 THE TRIGGER SYSTEM

## OBJECT RECONSTRUCTION IN THE ATLAS DETECTOR

---

5.1 ELECTRONS

5.2 PHOTONS

5.3 MUONS

5.4 JETS

5.5 MISSING TRANSVERSE ENERGY

5.6 MONTE CARLO SIMULATION



## APPLICATION OF A NEURAL NETWORK TO PIXEL CLUSTERING

### 6.1 CLUSTERING IN THE PIXEL DETECTOR

Creating tracks from individual hits in the Inner Detector is one of most computationally challenging parts of the reconstruction of ATLAS events. Each event typically contains thousands of hits in the pixel detector alone, which must be combined into one coherent picture of which particles traversed the detector, and how they moved and lost energy as they traveled. A typical particle deposits charge in several pixels per layer, forming a series of clusters which can be connected together to form a track. This track can in turn be used to measure the charge, momentum, and trajectory of the particle, and in many cases, provides ATLAS's most precise measurement of a charged particle.

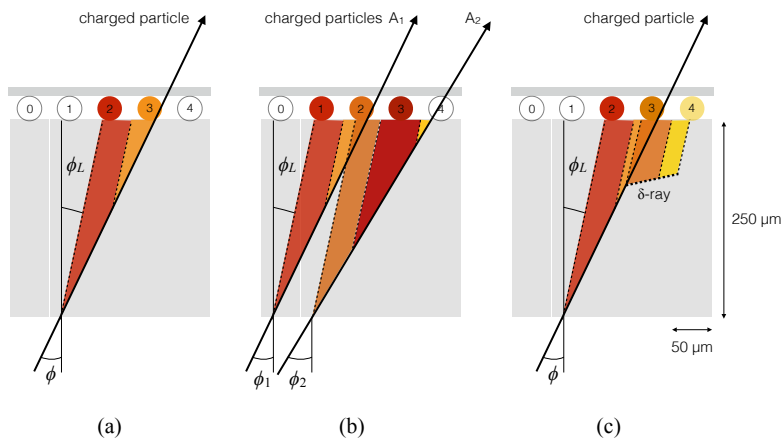


Figure 9: A few possible types of clusters in the Pixel Detector. (a) shows a single particle passing through a layer of the detector, (b) shows two particles passing through the detector, creating a single merged cluster, and (c) shows a single particle emitting a  $\delta$ -ray as it passes through the detector.

The process of going from clusters to track is relatively simple in an isolated environment in which one particle travels cleanly through all the layers, but can be complicated by multiple close-by tracks and by a single particle's emission of low energy particles, called  $\delta$ -rays. In these cases, it can be hard to tell how many particles were involved in creating a cluster, and where exactly each of those particles passed through the layer. A few examples of these cases can be seen in Fig-

ure 9 . The process of determining this is called Clustering, and it has recently been updated from a charge interpolation method to a method using a NN.

#### 6.1.1 Charge Interpolation Method

A typical cluster contains a few pixel hits spanning in the  $x$  and  $y$  directions, each with its own measurement of charge deposition, or Time Over Threshold (ToT). The extent of the cluster is defined by grouping together any pixels with a shared edge or corner. In the charge interpolation method, also called the CCA clustering algorithm, these individual hits are combined to make one estimation of the position a single particle which passed through them, using the following equation:

$$x_{cluster} = x_{center} + \Delta_x(\phi, N_{row}) \cdot \left[ \Omega_x - \frac{1}{2} \right] \quad (14)$$

$$x_{cluster} = x_{center} + \Delta_x(\phi, N_{row}) \cdot \left[ \Omega_x - \frac{1}{2} \right] \quad (15)$$

where  $\Omega_{x(y)}$  is defined by

$$\Omega_{x(y)} = \frac{q_{last\ row(col)}}{q_{first\ row(col)} + q_{last\ row(col)}} \quad (16)$$

and  $q$  represents the ToT of a given pixel, and  $\Delta_{x(y)}$  is a function derived from either data or Monte Carlo (MC) and produces an output related to the projected length of the particles track on the pixel sensor and is measured as a function of  $\phi$ , the incident angle of a particle on the sensor, and  $N_{row(col)}$ , the number of pixels in the  $x$  and  $y$  direction.

In a simple case, such as (a) of Figure 9 , this method works quite effectively. However, in cases like (b), it has no ability distinguish two-particle from one-particle clusters, and can only assign a cluster center between the two particles' locations, despite that intermediate pixel having the lowest ToT. Furthermore, because this method can't differentiate two-particle clusters, the tracking software can't use that information to preferentially allow multiple tracks to be fit to the cluster. In cases like (c), the  $\delta$ -ray will bias the measurement of the particle's position in whichever direction it is emitted.

#### 6.1.2 Improving Measurement with Neural Networks

To address these problems, a series of NNs were created [3]. The first determines the number of particles in a given cluster, the second predicts their positions with the cluster, and the third assesses the resolution of the position measurement.

These NNs are all trained with:



- a  $7 \times 7$  grid of cluster [ToT](#) information<sup>1</sup>
- a seven-element vector containing the  $y$ -size of the pixels in the grid
- the layer number of the cluster
- a variable indicating whether the cluster located in the barrel or endcap
- $\theta$  and  $\phi$  variables projecting the incident angles of the particle on the sensor, assuming it comes from the interaction point
- the  $\eta$  index of the pixel module

After the Number [NN](#) predicts a number of particles associated with the cluster, required to be between 1 and 3, the same inputs are fed to one of three Position [NNs](#) based on the determined number of particles, which then outputs the  $x$  and  $y$  positions of each of the particles. Then, the same inputs combined with the output of the Position [NN](#) are fed into one of three Error [NNs](#) (also distinguished by number of particles), which outputs a resolution for each of the position predictions made. An example of the output of this process can be seen in [Figure 10](#), where the improved position resolution from the ability to identify a multi-particle cluster is evident. The particle location predictions from the [NNs](#) are then handed to the tracking software, which is able to independently consider multiple locations from a given cluster to find the best fit.

## 6.2 IMPACT OF THE NEURAL NETWORK

The [NN](#) was first applied to  $7\text{TeV}$  data, where it improved position resolution for particles in small and large clusters. [Figure 11](#) shows the improvement from the addition of the [NN](#) in  $x$  resolution in different cluster sizes. The improvement from [CCA](#) clustering is particularly evident in the 4-pixel case, where the double peaked structure of the interpolation method has been completely removed with the [NN](#).

### 6.2.1 The Neural Network in $13\text{ TeV}$ Data

In Run 2, tracking algorithm is first run on the [CCA](#) clusters, where it constructs loose tracks that allow shared clusters, clusters to which multiple tracks are fit. The [NN](#) is then used to identify which clusters are likely to have had multiple particles pass through them, and to identify the positions of those particles. In the case that the cluster is

<sup>1</sup> Clusters spanning more than seven pixels in either direction are split into multiple clusters.

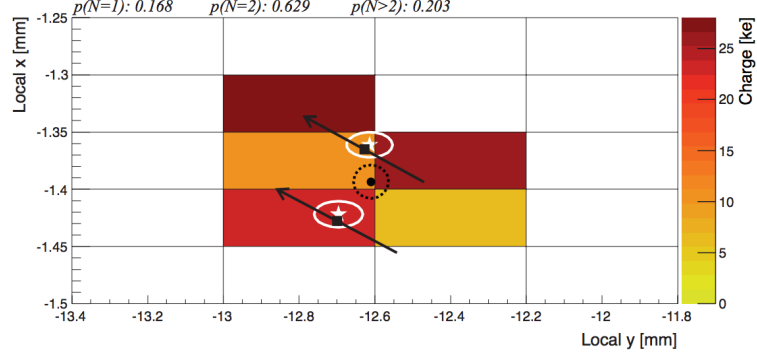


Figure 10: One example of a two-particle cluster and its truth information compared with the output of the NNs. At top, the  $p(N = i)$  values give the output of the Number NN, the probabilities that the cluster contains 1, 2, and 3 particles. Given the highest probability is for  $N = 2$ , the other NNs predict the position and errors of the two particles (in white). The black arrows and squares represent the truth information from the cluster, and the black dot and dotted line show the position measurement for the un-split cluster.

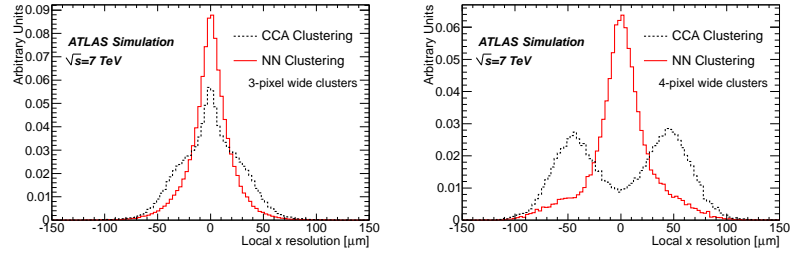


Figure 11:  $x$  resolutions for clusters with 3 (left) and 4 (right) pixels in the  $x$  direction in 7 TeV data for CCA and NN clustering.

determined to have resulted only from one particle, tracks that share that cluster are penalized.

Performance in 13 TeV [4].

Robustness [5]

## Part IV

### SEARCHING FOR SUPERSYMMETRY

This section describes an analysis of the ATLAS data carried out by the author and her analysis team. The analysis was performed on events from  $p - p$  collisions provided by the [LHC](#) at  $\sqrt{s}=13$  TeV. It searches for events like those described in [Section 2.2.3.1](#), which contain a Z boson decaying to leptons, jets, and missing transverse energy. The selection of a signal region in which to search for these events, background estimates, systematic uncertainty estimates, results, and interpretations are all discussed.



## BACKGROUND PROCESSES

This analysis is fundamentally a search for Supersymmetry in events with two leptons whose invariant mass is consistent with a Z boson. Additional event selections are made to reduce Standard Model processes relative to potential Supersymmetric processes, defined by simplified models discussed in [Section 2.2.3.1](#). Supersymmetric events typically have large amounts of  $E_T^{\text{miss}}$ ,  $H_T$  (the scalar sum of the  $p_T$  of objects in the event), and many jets. All of these features can help isolate these events from backgrounds. To understand what cuts would optimize the sensitivity of the search, it is essential to first understand what these Standard Model backgrounds are.

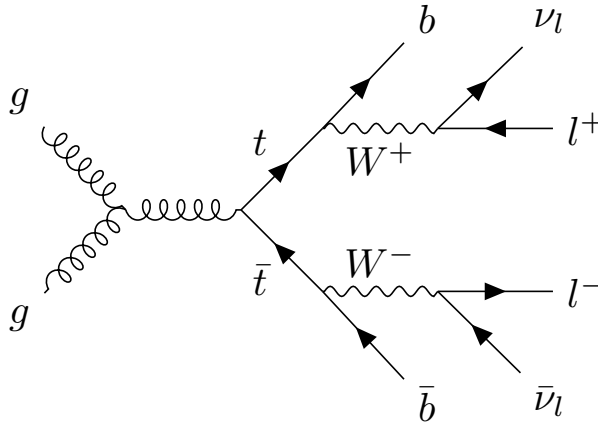


Figure 12: An example Feynman diagram of  $t\bar{t}$  production and decay.

$t\bar{t}$  is the largest background for this search. [Figure 12](#) shows an example of this process, which can decay to many jets, leptons, and neutrinos, which are seen in the detector as  $E_T^{\text{miss}}$ . Thus,  $t\bar{t}$  naturally has high  $E_T^{\text{miss}}$  and  $H_T$ , jets, and leptons from two different W boson decays, which may coincidentally form an invariant mass on the Z peak. These events are very difficult to separate from potential signals, though keeping the mass window small and increasing  $E_T^{\text{miss}}$  and  $H_T$  above the typical values for  $t\bar{t}$  events can help reduce them.

**DIBOSON** production is the next leading background. These events can contain real Z bosons and will peak on-Z like a signal. In addition, in events like [Figure 13](#), an additional W boson can decay to another lepton and a neutrino, providing  $E_T^{\text{miss}}$ . The pictured process can occur with associated jets, but at reduced rates, so adding a jet requirement to the signal region can help reduce these events. If the

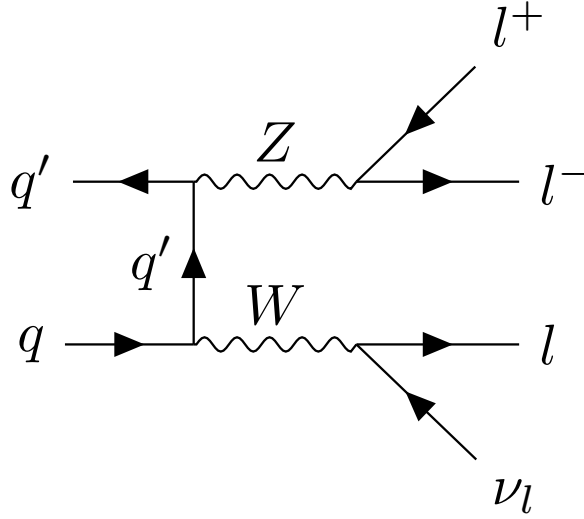


Figure 13: An example Feynman diagram of the production and decay of a WZ event.

W boson in this diagram instead decayed to two jets, there would be no true  $E_T^{\text{miss}}$  from a neutrino, so a  $E_T^{\text{miss}}$  cut in conjunction with a jet cut is very effective in reducing the total diboson background.

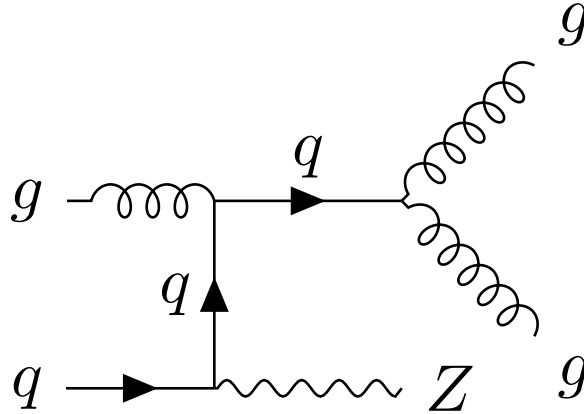


Figure 14: An example Feynman diagram of the production and decay of a  $Z/\gamma^* + \text{jets}$  event.

$Z/\gamma^* + \text{JETS}$  processes are very common but, as shown in [Figure 14](#), don't produce any true  $E_T^{\text{miss}}$  or a very large number of jets. Thus a high  $H_T$  cut can help reduce this background, but a  $E_T^{\text{miss}}$  cut is the most powerful. Events with very mismeasured jets or leptons can fake high  $E_T^{\text{miss}}$ , but these drastic mismeasurements are rare.

Other processes can contribute to the Standard Model background at lower rates. Processes similar to  $Z/\gamma^* + \text{jets}$  but with a W boson instead of a Z have real  $E_T^{\text{miss}}$  from leptonic W decays, but only one

lepton. However, a fake or non-prompt lepton can cause these events to look very similar to simulated signals. Additionally, there are rare processes such as  $t\bar{t}$  in association with bosons that will also be difficult to separate from signal processes.

## 7.1 MONTE CARLO SAMPLES

To precisely compare simulated signal to backgrounds, MC samples are generated for each of these processes. [Table 1](#) details the method used to produce each sample. With these and the simulated background, optimizations on a signal region can be made to maximize potential for discovery or exclusion of simplified Supersymmetric models. These comparisons and the signal region definition can be found in [Section 9.1](#).

Table 1: Simulated background event samples used in this analysis with the corresponding matrix element and parton shower generators, cross-section order in  $\alpha_s$  used to normalise the event yield, underlying-event tune and PDF set.

Physics process	Generator	Parton Shower	Cross section	Tune	PDF set
$t\bar{t} + W$ and $t\bar{t} + Z$ [6, 20]	MG5_AMC@NLO	Pythia 8.186	NLO [13, 24]	A14	NNPDF23LO
$t\bar{t} + WW$ [6]	MG5_AMC@NLO	Pythia 8.186	LO [10]	A14	NNPDF23LO
$t\bar{t}$ [9]	Powheg Box v2 r3026	Pythia 6.428	NNLO+NNLL [17, 18]	Perugia2012	NLO CT10
Single-top ( $Wt$ ) [9]	Powheg Box v2 r2856	Pythia 6.428	Approx. NNLO [23]	Perugia2012	NLO CT10
$WW$ ,	SHERPA 2.1.1	SHERPA 2.1.1	NNLO [12, 14]	SHERPA default	NLO CT10
$WZ$ and $ZZ$ [8]	SHERPA 2.1.1	SHERPA 2.1.1	NNLO [15, 16]	SHERPA default	NLO CT10
$Z/\gamma^*(\rightarrow \ell\ell) + \text{jets}$ [7]	SHERPA 2.1.1	SHERPA 2.1.1	NNLO [15, 16]	SHERPA default	NLO CT10



## OBJECT IDENTIFICATION AND SELECTION

---

8.1 ELECTRONS

8.2 MUONS

8.3 JETS

8.4 PHOTONS



## EVENT SELECTION

Table 2: Overview of all signal, control and validation regions used in the on-shell Z search. More details are given in the text. The flavour combination of the dilepton pair is denoted as either “SF” for same-flavour or “DF” for different flavour. All regions require at least two leptons, unless otherwise indicated. In the case of CR $\gamma$ , VR-WZ, VR-ZZ, and VR-3L the number of leptons, rather than a specific flavour configuration, is indicated. The main requirements that distinguish the control and validation regions from the signal region are indicated in bold. Most of the kinematic quantities used to define these regions are discussed in the text. The quantity  $m_T(\ell_3, E_T^{\text{miss}})$  indicates the transverse mass formed by the  $E_T^{\text{miss}}$  and the lepton which is not assigned to either of the Z-decay leptons.

On-shell Z regions	$E_T^{\text{miss}}$ [GeV]	$H_T^{\text{incl}}$ [GeV]	$n_{\text{jets}}$	$m_{\ell\ell}$ [GeV]	SF/DF	$\Delta\phi(\text{jet}_{12}, p_T^{\text{miss}})$	$m_T(\ell_3, E_T^{\text{miss}})$ [GeV]	$n_{\text{b-jets}}$
Signal region								
SRZ	$> 225$	$> 600$	$\geq 2$	$81 < m_{\ell\ell} < 101$	SF	$> 0.4$	—	—
Control regions								
CRZ	$< \mathbf{60}$	$> 600$	$\geq 2$	$81 < m_{\ell\ell} < 101$	SF	$> 0.4$	—	—
CR-FS	$> 225$	$> 600$	$\geq 2$	$\mathbf{61} < m_{\ell\ell} < \mathbf{121}$	<b>DF</b>	$> 0.4$	—	—
CRT	$> 225$	$> 600$	$\geq 2$	$> \mathbf{40}, m_{\ell\ell} \notin [\mathbf{81}, \mathbf{101}]$	SF	$> 0.4$	—	—
CR $\gamma$	—	$> 600$	$\geq 2$	—	$0\ell, 1\gamma$	—	—	—
Validation regions								
VRZ	$< \mathbf{225}$	$> 600$	$\geq 2$	$81 < m_{\ell\ell} < 101$	SF	$> 0.4$	—	—
VRT	$\mathbf{100-200}$	$> 600$	$\geq 2$	$> \mathbf{40}, m_{\ell\ell} \notin [\mathbf{81}, \mathbf{101}]$	SF	$> 0.4$	—	—
VRS	$\mathbf{100-200}$	$> 600$	$\geq 2$	$81 < m_{\ell\ell} < 101$	SF	$> 0.4$	—	—
VR-FS	$\mathbf{100-200}$	$> 600$	$\geq 2$	$\mathbf{61} < m_{\ell\ell} < \mathbf{121}$	<b>DF</b>	$> 0.4$	—	—
VR-WZ	$\mathbf{100-200}$	—	—	—	$3\ell$	—	$< 100$	0
VR-ZZ	$< 100$	—	—	—	$4\ell$	—	—	0
VR-3L	$\mathbf{60-100}$	$> \mathbf{200}$	$\geq 2$	$81 < m_{\ell\ell} < 101$	$3\ell$	$> 0.4$	—	—

## 9.1 SIGNAL REGION

## 9.2 CONTROL AND VALIDATION REGIONS

Trigger	L1	Notes
Single electron triggers		
HLT_e60_lhmedium	L1_EM22VHI	2015 and 2016
HLT_e60_lhmedium_nod0	L1_EM22VHI	2016 Only
HLT_e26_lhtight_nod0_ivarloose	L1_EM22VHI	Isolated; for evaluation in 2016
Di-electron triggers		
HLT_2e12_lhloose	L1_2EM13VH	2015 Only
HLT_2e17_lhvloose_nod0	L1_EM15VH	2016 Only
Single muon triggers		
HLT_mu50	L1_MU20	2015 and 2016
Di-muon triggers		
HLT_mu18_mu8noL1	L1_MU15	2015 Only
HLT_2mu14_nomucomb	L1_MU10	2016 Only
Electron-muon triggers		
HLT_e17_lhloose_mu14	L1_EM15VH_MU10	2015 Only
HLT_e7_lhmedium_mu24	L1_MU20	2015 Only
HLT_e17_lhloose_nod0_mu14	L1_MU10_EM15VH	2016 Only
HLT_e7_lhmedium_nod0_mu24	L1_MU20	2016 Only

Table 3: List of the triggers considered for this analysis. The corresponding L1 items are included for reference. The last column notes if the trigger is available in data.

Lepton $p_T$	Trigger in 2015	Trigger in 2016
Di-electron channel		
$p_T(e_1) > 65$ GeV	HLT_e60_lhmedium	HLT_e60_lhmedium_nod0
$p_T(e_1) \leq 65$ GeV	HLT_2e17_lhloose	HLT_2e17_lhvloose_nod0
Di-muon channel		
$p_T(\mu_1) > 52.5$ GeV	HLT_mu50	HLT_mu50
$p_T(\mu_1) \leq 52.5$ GeV	HLT_mu24_mu8noL1	HLT_2mu14_nomucomb
Electron-muon channel		
$p_T(e) > 65$ GeV	HLT_e60_lhmedium	HLT_e60_lhmedium_nod0
$p_T(e) \leq 65$ GeV and $p_T(\mu) > 52.5$ GeV	HLT_mu50	HLT_mu50
$p_T(e) \leq 65$ GeV and $p_T(\mu) \leq 52.5$ GeV and $p_T(e) < p_T(\mu)$	HLT_e7_lhmedium_mu24	HLT_e7_lhmedium_nod0_mu24
$p_T(e) \leq 65$ GeV and $p_T(\mu) \leq 52.5$ GeV and $p_T(\mu) < p_T(e)$	HLT_e17_lhloose_mu14	HLT_e17_lhloose_nod0_mu14

Table 4: Lepton trigger requirements used for the analysis in different regions of lepton- $p_T$  phase space.

## BACKGROUND ESTIMATION

---

This analysis requires two leptons that reconstruct to a  $Z$  mass, jets,  $E_T^{\text{miss}}$ , and  $H_T$ . Any standard model processes that produce this signature will appear as a background to the search. The most important task of the analysis is to identify and estimate these backgrounds, so that any excess of events appearing on top of the standard model background can be identified. The main backgrounds for this analysis are described in [Chapter 7](#). The largest background is from flavor symmetric processes, with smaller contributions coming from diboson processes,  $Z/\gamma^* + \text{jets}$ , rare top processes, and fake and non-prompt leptons.

### 10.1 FLAVOR SYMMETRIC PROCESSES

Flavor Symmetric (FS) backgrounds include any processes that produce pairs of leptons with uncorrelated flavor in the final state. In this analysis, the largest contribution comes from  $t\bar{t}$ , with additional events from processes like  $WW$  and  $Z \rightarrow \tau\tau$ . In these processes, each lepton comes from a different decay. Unlike a  $Z \rightarrow \ell\ell$  decay then, these leptons' flavors are completely independent.

#### 10.1.1 Flavor Symmetry Method

As a consequence of the independence of the lepton flavors, any FS process should produce  $ee$ ,  $\mu\mu$ , and  $e\mu$  events in a 1:1:2 ratio. This ratio is taken advantage of by the flavor symmetry method by measuring  $e\mu$  events in data and using them to predict the contribution of these processes in the  $ee$  and  $\mu\mu$  channels.

To estimate the number of events in SRZ, a control region called CR-FS is used. Both regions are defined in [Table 2](#). CR-FS is very similar to SRZ with two changes: it requires different-flavor leptons instead of the same-flavor leptons required by SRZ, and the  $m_{\ell\ell}$  range it covers has been expanded by a factor of three, now ranging from 61 to 121 GeV. The expansion of the  $m_{\ell\ell}$  window is done to increase the number of events in the control region, thus lowering the statistical uncertainty of the prediction<sup>1</sup>.

---

<sup>1</sup> Though this statistical uncertainty is no longer dominant for the analysis, the method was developed for a smaller dataset for which this expansion dramatically decreased the total uncertainty on the background prediction. [2] Because of previous excesses seen, the signal region was not reoptimized for the larger dataset used in this search,

This control region is expected to be about 95% pure in [FS](#) processes, with most of the remaining events coming from fake or non-prompt leptons. The [FS](#) portion is made up primarily of  $t\bar{t}$  ( $\sim 80\%$ ), with additional contributions from  $Wt$  ( $\sim 10\%$ ),  $WW$  ( $\sim 10\%$ ), and  $< 1\%$   $Z \rightarrow \tau\tau$ .

After the number of data events are measured in CR-FS, correction factors are applied to account for trigger efficiencies, selection efficiencies, the  $m_{\ell\ell}$  expansion, and the purity of the control region. Combining these factors, the estimate for number of events in the  $ee$  and  $\mu\mu$  channels is as follows:

$$N_{ee}^{\text{est}} = \frac{1}{2} \cdot f_{\text{FS}} \cdot f_{Z\text{-mass}} \cdot \sum_{e\mu}^{N_{e\mu}^{\text{data}}} k_e(p_T^\mu, \eta^\mu) \cdot \alpha(p_T^{\ell_1}, \eta^{\ell_1}), \quad (17)$$

$$N_{\mu\mu}^{\text{est}} = \frac{1}{2} \cdot f_{\text{FS}} \cdot f_{Z\text{-mass}} \cdot \sum_{e\mu}^{N_{e\mu}^{\text{data}}} k_\mu(p_T^e, \eta^e) \cdot \alpha(p_T^{\ell_1}, \eta^{\ell_1}), \quad (18)$$

where  $N_{e\mu}^{\text{data}}$  is the number of data events observed in CR-FS,  $k_e(p_T, \eta)$  and  $k_\mu(p_T, \eta)$  are relative selection efficiencies for electrons and muons, calculated in bins of  $p_T$  and  $\eta$  of the lepton to be replaced, and  $\alpha(p_T, \eta)$  accounts for the different trigger efficiencies for events in each channel, binned based on the kinematics of the leading lepton. These  $k$  and  $\alpha$  factors are calculated in an inclusive on- $Z$  selection ( $81 < m_{\ell\ell} / \text{GeV} < 101, \geq 2 \text{ jets}$ ), according to:

$$k_e(p_T, \eta) = \sqrt{\frac{N_{ee}^{\text{meas}}}{N_{\mu\mu}^{\text{meas}}}} \quad (19)$$

$$k_\mu(p_T, \eta) = \sqrt{\frac{N_{\mu\mu}^{\text{meas}}}{N_{ee}^{\text{meas}}}} \quad (20)$$

$$\alpha(p_T, \eta) = \frac{\sqrt{\epsilon_{ee}^{\text{trig}}(p_T, \eta) \times \epsilon_{\mu\mu}^{\text{trig}}(p_T, \eta)}}{\epsilon_{e\mu}^{\text{trig}}(p_T, \eta)} \quad (21)$$

where  $\epsilon_{ee/\mu\mu}^{\text{trig}}$  is the trigger efficiency <sup>2</sup> and  $N_{ee/\mu\mu}^{\text{meas}}$  is the number of  $ee/\mu\mu$  events in the inclusive on- $Z$  region described above. Here  $k_e(p_T, \eta) = 1/k_\mu(p_T, \eta)$ , and this  $k$  factor is calculated separately for leading and sub-leading leptons, and the appropriate  $k$  value is selected based on the position of the lepton to be replaced.

but in future iterations of this analysis, the signal region have tighter cuts, making this decreased statistical uncertainty significant once again.

<sup>2</sup> This efficiency is defined by taking all events in the inclusive on- $Z$  selection mentioned above and determining the fraction that passes the relevant trigger requirement defined by [Table 4](#). Because the offline selection made on these events already has some trigger dependence, this calculation of efficiency could be slightly biased. This effect is considered in [Section 11.1.1](#), and the uncertainty applied to the estimate as a result is described.

Region	$ee$ prediction	$\mu\mu$ prediction	combined prediction
Prediction for $14.7 \text{ fb}^{-1}$ of 2015+2016 Data			
SRZ	$16.50 \pm 2.11$	$16.67 \pm 2.04$	$33.16 \pm 3.94$
VRS	$49.70 \pm 4.61$	$49.60 \pm 4.56$	$99.31 \pm 8.47$

Table 5: Yields in signal and validation regions for the flavor symmetric background. Errors include statistical uncertainty, uncertainty from MC closure, uncertainty from the  $k$  and  $\alpha$  factors, uncertainty due to deriving triggers efficiencies from a DAOD, and uncertainty on the MC shape used to correct for the  $m_{\ell\ell}$  expansion.

Electron, muon, and trigger efficiencies are all quite close to one, and as a consequence, these correction factors are typically within 10% of unity, except in the region  $|\eta| < 0.1$  where, because of the lack of coverage of the muon spectrometer, they are up to 50% from unity.

The estimate is corrected for contamination of non-FS backgrounds in CR-FS. A scaling factor is determined by subtracting these backgrounds from the number of  $e\mu$  events measured in CR-FS, then determining the fraction of the original data events that this pure-FS number represents. The estimate for the other backgrounds is taken from MC for all processes except fakes, which are predicted from data using the matrix method described in Section 10.3.

A prediction is made both for the signal region, SRZ, and the lower- $E_T^{\text{miss}}$  validation region, VRS. This process is performed separately for the two data taking periods, 2015 and 2016, because of the changing triggers and conditions. The results are then summed together, as shown in Table 5. The uncertainties in this table are discussed in Section 11.1.1.

### 10.1.2 Sideband Fit Method

## 10.2 $Z/\gamma^* + \text{JETS BACKGROUND}$

### 10.3 FAKES

### 10.4 DIBOSONS

### 10.5 OTHER RARE PROCESSES





## SYSTEMATIC UNCERTAINTY

---

### 11.1 UNCERTAINTIES ON DATA-DRIVEN BACKGROUNDS

#### 11.1.1 *Uncertainties on the Flavor Symmetry Method*

The flavor symmetry method is a data driven method that makes its primarily on based events populating an Signal Region (SR)-like Control Region (CR) in the different-flavor channel. The statistical uncertainty on these events makes up the dominant uncertainty on the method. To reduce this uncertainty, the  $m_{\ell\ell}$  range on the CR is expanded, tripling the number of events in CR-FS. Though this reduces the statistical uncertainty significantly, it is still significantly higher than any of the other systematic uncertainties on this method, as seen in Table 6. Also included in the statistical uncertainty column is the uncertainty on the number of non-FS events in CR-FS, which is used to scale the prediction to remove any contamination in the CR.

The next largest contribution to the uncertainty comes from MC closure tests, which are used to determine how effective the method is in its prediction. If, for example, using weights derived from an inclusive selection at high  $E_T^{\text{miss}}$  lead to a bias, the closure test would indicate that and an appropriate uncertainty could be placed on the estimate based on the difference between the MC and the prediction. In this test, the entire FS procedure is performed on  $t\bar{t}$  MC, including a recalculation of weighting factors  $\alpha$  and  $k$ . The prediction from  $e\mu$  events in MC is compared to the MC  $ee$  and  $\mu\mu$  events, as seen in Figure 15. The difference between the two predictions is then summed in quadrature with the statistical uncertainty on each prediction to give the total closure uncertainty seen in Table 6. In these closure tests, all predictions agree within the statistical uncertainty, so the bulk of the resulting error is due to MC statistics.

A small uncertainty is added based on the statistical uncertainty on the  $k$  and  $\alpha$  factors derived from data. These factors are measured in many different bins (see, for example, the different measurements of  $k$  in Figure 16), and as a consequence, some bins can have very large statistical uncertainties. To assess the uncertainty on the total estimate, each measurement of these factors is varied by its uncertainty in order to produce the maximum and minimum possible prediction. This error is symmetrized, and the resulting change in the prediction is included in Table 6.

The next uncertainty considers a potential bias in the way the  $\alpha$  factors are calculated. Because they are derived from data, there is

Reg.	Ch.	Pred.	Uncertainties					
			stat.	MC clos.	k and $\alpha$	dAOD usage	$m_{\ell\ell}$ shape	total
SRZ	$ee$	16.50	1.82	0.88	0.53	0.12	0.22	2.11
	$\mu\mu$	16.67	1.83	0.79	0.33	0.11	0.23	2.04
	$ee+\mu\mu$	33.16	3.66	1.07	0.86	0.23	0.45	3.94
VRS	$ee$	49.70	3.21	2.34	2.20	0.34	0.75	4.61
	$\mu\mu$	49.60	3.14	2.88	1.40	0.31	0.75	4.56
	$ee+\mu\mu$	99.31	6.34	4.00	3.60	0.65	1.49	8.47

Table 6: Uncertainties in the on-Z signal and validation regions. Nominal predictions are given with statistical uncertainty (including uncertainty from subtracted backgrounds), MC Closure uncertainty, uncertainty on the prediction from varying  $k$  and  $\alpha$  by their statistical uncertainties, comparing the efficiencies from AODs to that of DAODs, and on the  $m_{\ell\ell}$  widening, which includes MC statistics and a data/MC comparison in a loosened region.

already trigger dependence in data collection (only events passing a trigger are stored) and further dependences is introduced by the use of the “dAOD” data format. This is short for derived **AOD!** (AOD!), and they provide smaller, more efficient versions of the complete ATLAS datasets. These dAODs are designed with specific analyses in mind, filtering on the triggers and objects required by the analyses. As a consequence, there are explicit requirements that lepton or  $E_T^{\text{miss}}$  triggers are passed before events are included in the dAODs used by this analysis. All of these

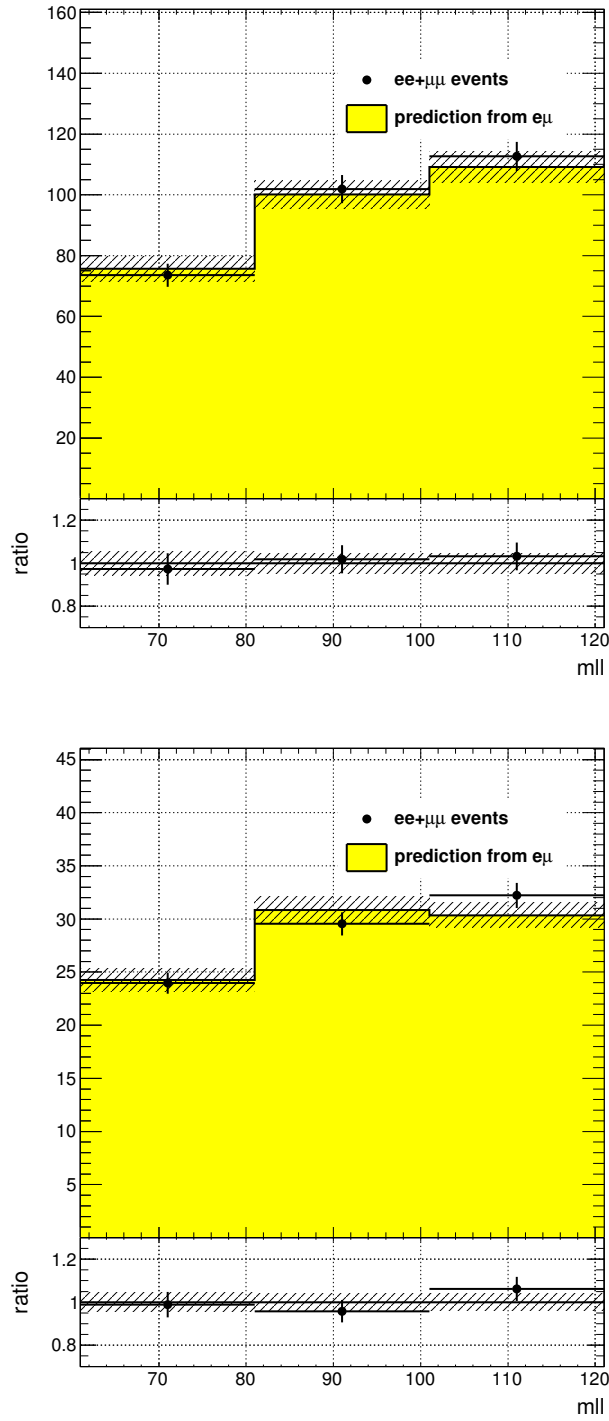


Figure 15: MC closure plots of VRS (top) and SRZ (bottom). The number of events from MC (black points) is compared to the number of events predicted from the flavor symmetry method (yellow histogram). The comparison is performed before the expanded  $m_{\ell\ell}$  window is used to predict the on-Z bin.

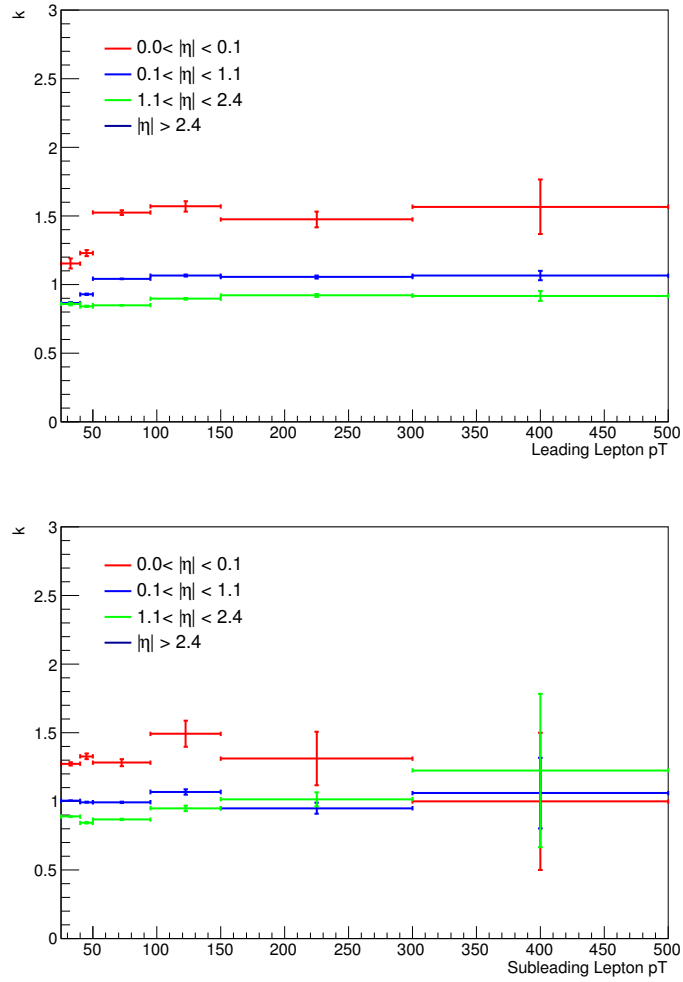


Figure 16: Measurements of  $k$ , the ratio of electron to muon events, in bins of  $p_T$  and  $\eta$ . On the top is the measurements indexed by the leading lepton, while the measurements indexed by the subleading lepton are on the bottom.

## RESULTS

---









## Part V

# CONCLUSIONS

This section presents conclusions and an outlook for future work.



## CONCLUSIONS

---







Part VI

APPENDIX





## APPENDIX TEST

Aliquam lectus. Vivamus leo. Quisque ornare tellus ullamcorper nulla. Mauris porttitor pharetra tortor. Sed fringilla justo sed mauris. Mauris tellus. Sed non leo. Nullam elementum, magna in cursus sodales, augue est scelerisque sapien, venenatis congue nulla arcu et pede. Ut suscipit enim vel sapien. Donec congue. Maecenas urna mi, suscipit in, placerat ut, vestibulum ut, massa. Fusce ultrices nulla et nisl.

Etiam ac leo a risus tristique nonummy. Donec dignissim tincidunt nulla. Vestibulum rhoncus molestie odio. Sed lobortis, justo et pretium lobortis, mauris turpis condimentum augue, nec ultricies nibh arcu pretium enim. Nunc purus neque, placerat id, imperdiet sed, pellentesque nec, nisl. Vestibulum imperdiet neque non sem accumsan laoreet. In hac habitasse platea dictumst. Etiam condimentum facilisis libero. Suspendisse in elit quis nisl aliquam dapibus. Pellentesque auctor sapien. Sed egestas sapien nec lectus. Pellentesque vel dui vel neque bibendum viverra. Aliquam porttitor nisl nec pede. Proin mattis libero vel turpis. Donec rutrum mauris et libero. Proin euismod porta felis. Nam lobortis, metus quis elementum commodo, nunc lectus elementum mauris, eget vulputate ligula tellus eu neque. Vivamus eu dolor.

## A.1 APPENDIX SECTION TEST

Nulla in ipsum. Praesent eros nulla, congue vitae, euismod ut, commodo a, wisi. Pellentesque habitant morbi tristique senectus et netus et malesuada fames ac turpis egestas. Aenean nonummy magna non leo. Sed felis erat, ullamcorper in, dictum non, ultricies ut, lectus. Proin vel arcu a odio lobortis euismod. Vestibulum ante ipsum primis in faucibus orci luctus et ultrices posuere cubilia Curae; Proin ut est. Aliquam odio. Pellentesque massa turpis, cursus eu, euismod nec, tempor congue, nulla. Duis viverra gravida mauris. Cras tincidunt. Curabitur eros ligula, varius ut, pulvinar in, cursus faucibus, augue.

*More dummy text*

Nulla mattis luctus nulla. Duis commodo velit at leo. Aliquam vulputate magna et leo. Nam vestibulum ullamcorper leo. Vestibulum condimentum rutrum mauris. Donec id mauris. Morbi molestie justo et pede. Vivamus eget turpis sed nisl cursus tempor. Curabitur mollis sapien condimentum nunc. In wisi nisl, malesuada at, dignissim sit amet, lobortis in, odio. Aenean consequat arcu a ante. Pellentesque porta elit sit amet orci. Etiam at turpis nec elit ultricies imperdiet. Nulla facilisi. In hac habitasse platea dictumst. Suspendisse

LABITUR BONORUM PRI NO	QUE VISTA	HUMAN
fastidii ea ius	germano	demonstratea
suscipit instructor	titulo	personas
quaestio philosophia	facto	demonstrated

Table 7: Autem usu id.

viverra aliquam risus. Nullam pede justo, molestie nonummy, scelerisque eu, facilisis vel, arcu.

## A.2 ANOTHER APPENDIX SECTION TEST

Curabitur tellus magna, porttitor a, commodo a, commodo in, tortor. Donec interdum. Praesent scelerisque. Maecenas posuere sodales odio. Vivamus metus lacus, varius quis, imperdiet quis, rhoncus a, turpis. Etiam ligula arcu, elementum a, venenatis quis, sollicitudin sed, metus. Donec nunc pede, tincidunt in, venenatis vitae, faucibus vel, nibh. Pellentesque wisi. Nullam malesuada. Morbi ut tellus ut pede tincidunt porta. Lorem ipsum dolor sit amet, consectetur adipiscing elit. Etiam congue neque id dolor.

Donec et nisl at wisi luctus bibendum. Nam interdum tellus ac libero. Sed sem justo, laoreet vitae, fringilla at, adipiscing ut, nibh. Maecenas non sem quis tortor eleifend fermentum. Etiam id tortor ac mauris porta vulputate. Integer porta neque vitae massa. Maecenas tempus libero a libero posuere dictum. Vestibulum ante ipsum primis in faucibus orci luctus et ultrices posuere cubilia Curae; Aenean quis mauris sed elit commodo placerat. Class aptent taciti sociosqu ad litora torquent per conubia nostra, per inceptos hymenaeos. Vivamus rhoncus tincidunt libero. Etiam elementum pretium justo. Vivamus est. Morbi a tellus eget pede tristique commodo. Nulla nisl. Vestibulum sed nisl eu sapien cursus rutrum.

There is also a useless Pascal listing below: [Listing 1](#).

Listing 1: A floating example (listings manual)

```

1 for i:=maxint downto 0 do
  begin
    { do nothing }
  end;
```

## BIBLIOGRAPHY

---

- [1] ATLAS Collaboration. “The ATLAS Experiment at the CERN Large Hadron Collider.” In: *JINST* 3 (2008), So8003. DOI: [10 . 1088/1748-0221/3/08/S08003](https://doi.org/10.1088/1748-0221/3/08/S08003).
- [2] ATLAS Collaboration. *Search for supersymmetry in final states with jets, missing transverse momentum and a Z boson at  $\sqrt{s} = 8$  TeV with the ATLAS detector*. ATLAS-CONF-2012-152. 2012. URL: <http://cds.cern.ch/record/1493491>.
- [3] ATLAS Collaboration. “A neural network clustering algorithm for the ATLAS silicon pixel detector.” In: *JINST* 9 (2014), P09009. DOI: [10 . 1088 / 1748 - 0221 / 9 / 09 / P09009](https://doi.org/10.1088/1748-0221/9/09/P09009). arXiv: [1406 . 7690 \[hep-ex\]](https://arxiv.org/abs/1406.7690).
- [4] ATLAS Collaboration. *Measurement of performance of the pixel neural network clustering algorithm of the ATLAS experiment at  $\sqrt{s} = 13$  TeV*. ATL-PHYS-PUB-2015-044. 2015. URL: <http://cdsweb.cern.ch/record/2054921>.
- [5] ATLAS Collaboration. *Robustness of the Artificial Neural Network Clustering Algorithm of the ATLAS experiment*. ATL-PHYS-PUB-2015-052. 2015. URL: <http://cdsweb.cern.ch/record/2116350>.
- [6] ATLAS Collaboration. *Modelling of the  $t\bar{t}H$  and  $t\bar{t}V$  ( $V = W, Z$ ) processes for  $\sqrt{s} = 13$  TeV ATLAS analyses*. ATL-PHYS-PUB-2016-005. 2016. URL: <http://cds.cern.ch/record/2120826>.
- [7] ATLAS Collaboration. *Monte Carlo Generators for the Production of a W or Z/ $\gamma^*$  Boson in Association with Jets at ATLAS in Run 2*. ATL-PHYS-PUB-2016-003. 2016. URL: <http://cds.cern.ch/record/2120133>.
- [8] ATLAS Collaboration. *Multi-Boson Simulation for 13 TeV ATLAS Analyses*. ATL-PHYS-PUB-2016-002. 2016. URL: <http://cds.cern.ch/record/2119986>.
- [9] ATLAS Collaboration. *Simulation of top quark production for the ATLAS experiment at  $\sqrt{s} = 13$  TeV*. ATL-PHYS-PUB-2016-004. 2016. URL: <http://cds.cern.ch/record/2120417>.
- [10] J. Alwall, R. Frederix, S. Frixione, V. Hirschi, F. Maltoni, O. Mattelaer, H. S. Shao, T. Stelzer, P. Torrielli, and M. Zaro. “The automated computation of tree-level and next-to-leading order differential cross sections, and their matching to parton shower simulations.” In: *JHEP* 07 (2014), p. 079. DOI: [10 . 1007/JHEP07\(2014\)079](https://doi.org/10.1007/JHEP07(2014)079). arXiv: [1405.0301 \[hep-ph\]](https://arxiv.org/abs/1405.0301).

- [11] C. P. Burgess and G. D. Moore. *The standard model: A primer*. Cambridge University Press, 2006. ISBN: 9780511254857, 9781107404267, 9780521860369.
- [12] J. M. Campbell and R. K. Ellis. “An update on vector boson pair production at hadron colliders.” In: *Phys. Rev. D* 60 (1999), p. 113006. arXiv: [hep-ph/9905386](#) [[hep-ph](#)].
- [13] J. M. Campbell and R. K. Ellis. “ $t\bar{t}$  W production and decay at NLO.” In: *JHEP* 1207 (2012), p. 052. arXiv: [1204.5678](#) [[hep-ph](#)].
- [14] J. M. Campbell, R. K. Ellis, and C. Williams. “Vector boson pair production at the LHC.” In: *JHEP* 1107 (2011), p. 018. arXiv: [1105.0020](#) [[hep-ph](#)].
- [15] S. Catani and M. Grazzini. “An NNLO subtraction formalism in hadron collisions and its application to Higgs boson production at the LHC.” In: *Phys. Rev. Lett.* 98 (2007), p. 222002. arXiv: [hep-ph/0703012](#) [[hep-ph](#)].
- [16] S. Catani, L. Cieri, G. Ferrera, D. de Florian, and M. Grazzini. “Vector boson production at hadron colliders: a fully exclusive QCD calculation at NNLO.” In: *Phys. Rev. Lett.* 103 (2009), p. 082001. arXiv: [0903.2120](#) [[hep-ph](#)].
- [17] M. Czakon, P. Fiedler, and A. Mitov. “Total Top-Quark Pair-Production Cross Section at Hadron Colliders Through  $O(\alpha_s^4)$ .” In: *Phys. Rev. Lett.* 110 (2013), p. 252004. arXiv: [1303.6254](#) [[hep-ph](#)].
- [18] M. Czakon and A. Mitov. “Top++: A Program for the Calculation of the Top-Pair Cross-Section at Hadron Colliders.” In: *Comput. Phys. Commun.* 185 (2014), p. 2930. DOI: [10.1016/j.cpc.2014.06.021](#). arXiv: [1112.5675](#) [[hep-ph](#)].
- [19] D. Galbraith.
- [20] M. V. Garzelli, A. Kardos, C. G. Papadopoulos, and Z. Trocsanyi. “ $t\bar{t} W^{+-}$  and  $t\bar{t} Z$  Hadroproduction at NLO accuracy in QCD with Parton Shower and Hadronization effects.” In: *JHEP* 11 (2012), p. 056. DOI: [10.1007/JHEP11\(2012\)056](#). arXiv: [1208.2665](#) [[hep-ph](#)].
- [21] David J Griffiths. *Introduction to elementary particles; 2nd rev. version*. Physics textbook. New York, NY: Wiley, 2008. URL: [https://cds.cern.ch/record/111880](#).
- [22] Huang, Qing-Guo, Wang, Ke, and Wang, Sai. “Constraints on the neutrino mass and mass hierarchy from cosmological observations.” In: *Eur. Phys. J. C* 76.9 (2016), p. 489. DOI: [10.1140/epjc/s10052-016-4334-z](#). URL: [http://dx.doi.org/10.1140/epjc/s10052-016-4334-z](#).

- [23] N. Kidonakis. “Two-loop soft anomalous dimensions for single top quark associated production with a  $W^-$  or  $H^-$ .” In: *Phys. Rev. D* 82 (2010), p. 054018. DOI: [10.1103/PhysRevD.82.054018](https://doi.org/10.1103/PhysRevD.82.054018). arXiv: [1005.4451](https://arxiv.org/abs/1005.4451) [hep-ph].
- [24] A. Lazopoulos, T. McElmurry, K. Melnikov, and F. Petriello. “Next-to-leading order QCD corrections to  $t\bar{t}Z$  production at the LHC.” In: *Phys. Lett. B* 666 (2008), p. 62. arXiv: [0804.2220](https://arxiv.org/abs/0804.2220) [hep-ph].
- [25] A. D. Martin, W. J. Stirling, R. S. Thorne, and G. Watt. “Parton distributions for the LHC.” In: (2009). DOI: [10.1140/epjc/s10052-009-1072-5](https://doi.org/10.1140/epjc/s10052-009-1072-5). eprint: [arXiv:0901.0002](https://arxiv.org/abs/0901.0002).
- [26] Johan Messchendorp. “Physics with Charmonium – A few recent highlights of BESIII.” In: *PoS Bormio2013* (2013), p. 043. arXiv: [1306.6611](https://arxiv.org/abs/1306.6611) [hep-ex].
- [27] F. Zwicky. “Die Rotverschiebung von extragalaktischen Nebeln.” In: *Helvetica Physica Acta* 6 (1933), 110–127.
- [28] LHCb collaboration. “Observation of  $J/\Psi p$  resonances consistent with pentaquark states in  $\Lambda_b^0 \rightarrow J/\Psi K^- p$  decays.” In: (2015). DOI: [10.1103/PhysRevLett.115.072001](https://doi.org/10.1103/PhysRevLett.115.072001). eprint: [arXiv:1507.03414](https://arxiv.org/abs/1507.03414).
- [29] T. S. van Albada, J. N. Bahcall, K. Begeman, and R. Sancisi. “Distribution of dark matter in the spiral galaxy NGC 3198.” In: *The Astrophysical Journal* 295 (Aug. 1985), pp. 305–313. DOI: [10.1086/163375](https://doi.org/10.1086/163375).